Shahrood University of Technology

Journal of Hydraulic and Water Engineering (JHWE)

Journal homepage: https://jhwe.shahroodut.ac.ir

Iranian Hydraulic Association (IHA)

A Hybrid Solution for Transient Pipe Flow based on Method of Characteristics and Lax-Friedrichs Scheme

Faeze Khalighi [1,2,*], Ahmad Ahmadi [1], Alireza Keramat [3,4], Arris Tijsseling [2]

[1] Department of Civil Engineering, Shahrood University of Technology, Shahrood, Iran.
[2] Department of Mathematics and Computer Science, Eindhoven University of Technology, P.O. Box 513, 5600 MB Eindhoven, The Netherlands.
[3] Department of Civil and Environmental Engineering, Hong Kong Polytechnic University, Hung Hom, SAR 999077, Kowloon, Hong Kong.
[4] Research Institute for Land and Space, Hong Kong Polytechnic University, Hung Hom SAR 999077, Kowloon, Hong Kong.

Article Info

Article history:

Received: 6 May 2023
Received in revised form: 6 Dec 2023
Accepted: 20 June 2024
Published online 22 June 2024

DOI:
10.22044/jhwe.2024.13086.1015

Keywords
Transient flow
Hybrid method
Method of characteristic
Two-step variant of Lax-Friedrichs
Water hammer
Fluid-structure interaction

Abstract

Method of Characteristics (MOC) has long been an excellent and widely established technique for analyzing transient flow, especially in a single pipeline with constant wave speed. But this method has some limitations in terms of mesh sizing while studying multi-pipe systems or systems with different wave speeds. More specifically, it needs all pipes to satisfy the Courant number to be unity while the same time step should be chosen for all pipes. With this, one reach in each pipe remains, which does not satisfy the Courant requirement. As one possible remedy to this shortcoming, a hybrid numerical method based on MOC and a two-step variant of the Lax-Friedrichs method (MOC-LF) is suggested in the present study. This method is compared against the conventional MOC scheme, which adapts interpolation for the remaining length per pipe (MOC-MOC). In the approach, two significant effects of fluid structure interaction (FSI) in fluid-filled tubes, namely Poisson and junction coupling, are introduced. The computational simulations are carried out for a reservoir-pipe-valve system with instantaneous and gradual closure of the downstream valve. The results of proposed scheme and those of MOC with interpolation are in good agreement with solutions obtained by MOC with a very fine grid, which are taken as a reference. Detailed comparison of the computational methods in terms of error indicates that the proposed MOC-LF can be a good alternative for conventional MOC schemes.

1. Introduction

Hydraulic transients, also called water hammer, are planned or unexpected changes in water pipe systems, e.g. by opening or closing a pump or valve. As a consequence, a pressure wave is formed, which travels back and forth in the pipeline. Pressure waves can generate axial displacements and stresses in the pipe walls due to Poisson coupling. In addition, unbalanced forces at a valve or a bend result in

* *Corresponding author:* faeze_khalighi@yahoo.com

the movement of pipes, known as junction coupling (Hosseini et al., 2020).

Transient hydraulic analysis is essential in designing and exploiting pressurized water pipe systems to guarantee their security, reliability, and good performance under abnormal operational conditions (Ramos et al., 2009). Numerical simulation has now become the main approach for transient analysis (Zhang et al., 2018). The essence of the water hammer calculation is to solve a set of hyperbolic partial differential equations. Many methods have been developed for transient analysis (for instance, El Idrissi et al. 2023; Lu et al. 2024; Wan et al. 2023; Shi et al. 2023; Zhang et al. 2023).

The method of Characteristics (MOC) is currently one of the most popular techniques due to its accuracy, simplicity, and ability to include different boundary conditions (Greyvenstein, 2002; Laguna and Tsouvalas, 2014). It is widely used to simulate water hammer complications in various engineering practices such as fluid structure interaction (FSI) (Ferras et al., 2018, Hosseini et al. 2020), unsteady friction (Ferras et al., 2017; Urbanowicz, 2018), viscoelasticity (Keramat et al., 2012; Henclik, 2018), and column separation (Bergant et al., 2006; Ghodhbani et al., 2019). Although the method is ideal for a single pipeline with constant wave speed, the requirement of strict adherence to the Courant time step-reach length relationship becomes a limitation for MOC in multi-pipe systems (Pal et al., 2021). It needs all pipes to satisfy the Courant number to be unity, and on the other hand, a common time step should be chosen throughout the time-domain computation. Figure 1 shows a series pipe system consisting of two pipes, pipe 1 (L_1,c_1) and pipe 2 (L_2,c_2). The same computational time step is used for two pipes. In the MOC approach, the unity of the Courant number (equations shown in the figure) should be satisfied. n_1 and n_2 are the number of reaches, and they should be integer. As shown, the second pipe cannot meet the introduced criterion. n_2 is not an integer, and the gray area remains unsolved. In this figure, there are only two pipes, and by playing with the spatial step, it is possible to solve the Courant number criterion, but a pipe network usually consists of several pipes, and it is impossible to satisfy this criterion for all pipes.

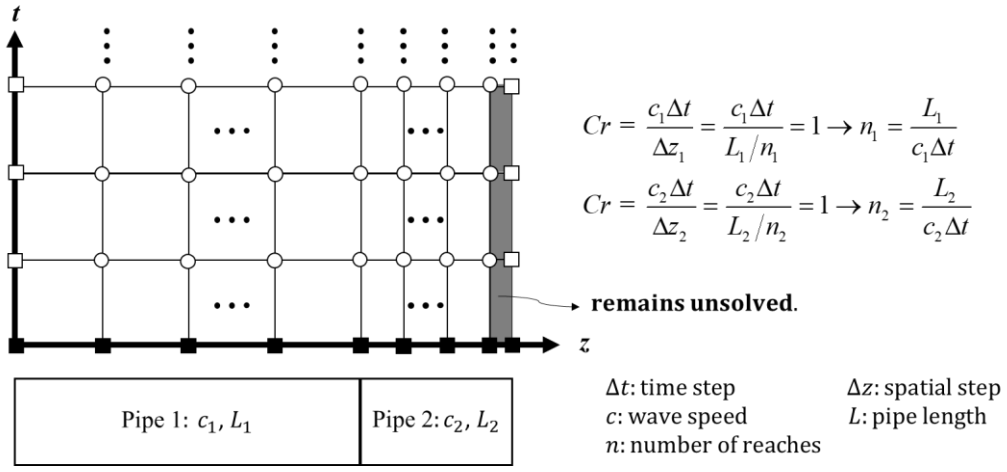

Figure 1. MOC limitation schematic.

One possible remedy to this shortcoming is using interpolation. Wiggert and Sundquist (1997) suggested an interpolation algorithm by coupling space-line interpolation and space reach out interpolation. Lai (1988) presents a method by the combination of different interpolation methods, and called it the multimode scheme. Shimada et al. (2006) proposed analytical predictions of numerical errors of both space-line and time-line interpolation methods. Ghidaoui et al. (1998) suggested an integrated-energy approach to explore the origins of discretization errors related to common space-line and time-line interpolation methods and how these errors can be managed. Interpolation is fundamentally non-physical and leads to numerical errors in the form of dissipation and dispersion (Pal et al., 2021).

Another solution is to use wave-speed adjustment. In the wave-speed adjustment approach, one of the pipeline properties (usually wave speed) is altered to meet the Courant requirement (Twyman, 2016). While adjusting the wave speed may seem straightforward because it is non-dispersive, requiring only a certain percentage modification to meet $Cr = 1$, it alters the physical properties of the problem (Ghidaoui and Karney, 1994; Twyman, 2016).

The next solution is that the water hammer is analyzed using a hybrid scheme that solves the transient flow by applying the MOC on those pipes with a Courant number equal to 1 and using another stable and accurate scheme on the disproportionate part of the pipes. Samani and Khayatzadeh (2002) coupled MOC and the implicit finite difference method (IFDM) for solving transient flow in pipe networks. The obtained numerical results had good agreement with the available exact analytical solutions for many test examples. Twyman (2017) proposed a hybrid numerical method based on MOC and IFDM. He analyzed the transient flow in two pipe networks; it is demonstrated that this solution-type allows obtaining high accuracy solution. However the IFDM implementation has a certain level of complexity. Moreover, it spends more computational memory and takes longer to complete the execution simulation time (Twyman, 2018).

As a conventional numerical method, the Lax-Friedrichs (LF) method is widely used in computational fluid dynamics (CFD). It is a straightforward method for the solution of hyperbolic partial differential equations (PDEs). Its use is limited because its order of accuracy is only one, but it is easy to program, applicable to general PDEs, and has good qualitative properties because it is monotone (Thomas, 1995; Shampine, 2004). Khalighi et al. (2016; 2017) reported the results of the two-step variant of Lax-Friedrichs in water hammer simulations. The LF method is confirmed as reliable in axial FSI problems compared to the exact solution of a system of four linear hyperbolic equations in a reservoir-pipe-valve system.

A hybrid numerical method based on MOC and the two-step variant of Lax-Friedrichs (MOC-LF) is proposed in the present study. A frictionless reservoir-pipe-valve system with both sudden and gradual valve-closure patterns is taken as the test problem. In the implementation, a single pipeline is divided into two reaches. This system is chosen because it describes a clear representation of the solution for a simple series network. The results are compared against the MOC with a very fine grid to verify the accuracy and report on the root mean squared deviation (RMSD) of the studied schemes.

2. Materials and Methods

2.1. Governing equations

The pipe under consideration is horizontal, thin-walled, linearly elastic, and filled with a weakly compressible fluid. The radial inertia and radial shear deformation of the pipe wall are neglected. The other structural assumptions are that there is no buckling and that the deformations are small. The hydraulic equations and structural equations without

considering friction are (Tijsseling, 2003; Keramat et al., 2012):

$$\frac{\partial V}{\partial z}+\frac{g}{{c_f}^2}\frac{\partial H}{\partial t}-2\upsilon\frac{\partial \dot{u}_z}{\partial z}=0 \quad (1)$$

$$\frac{\partial V}{\partial t}+g\frac{\partial H}{\partial z}=0 \quad (2)$$

in which:

$$c_f=(\rho_f(\frac{1}{K}+\frac{D}{eE}(1-\upsilon^2)))^{-0.5} \quad (3)$$

where V=fluid velocity, H= fluid pressure head, g=gravitational acceleration, c_f = pressure wave speed, υ =Poisson's ratio, E= Young's modulus for pipe wall material, $\dot{u}_z$ = axial pipe velocity, D=inner pipe diameter, K = fluid bulk modulus, ρ_f = fluid density, and e = pipe wall thickness.

The governing equations for the axial motion of the pipe are similar to Eqs. (1), (2), and (3):

$$\frac{\partial \dot{u}_z}{\partial z}-\frac{1}{\rho_t {c_t}^2}\frac{\partial \sigma_z}{\partial t}+g\frac{D}{2}\frac{\upsilon\rho_f}{eE}\frac{\partial H}{\partial t}=0 \quad (4)$$

$$\frac{\partial \dot{u}_z}{\partial t}-\frac{1}{\rho_t}\frac{\partial \sigma_z}{\partial z}=0 \quad (5)$$

in which:

$$c_t^2=E/\rho_t \quad (6)$$

where σ_z =axial pipe stress, ρ_t =density of pipe wall material, and c_t=axial stress wave speed.

The governing equations can be written in the following form:

$$\mathbf{A}\frac{\partial \mathbf{y}}{\partial t}+\mathbf{B}\frac{\partial \mathbf{y}}{\partial z}=0 \quad (7)$$

where **y** is the vector of unknowns, and **A** and **B** are matrices of constant coefficients:

$$\mathbf{y}=\begin{Bmatrix} V \\ H \\ \dot{u}_z \\ \sigma_z \end{Bmatrix}, \quad (8)$$

$$\mathbf{A}=\begin{bmatrix} 1 & 0 & 0 & 0 \\ 0 & \frac{g}{c_f^2} & 0 & 0 \\ 0 & 0 & 1 & 0 \\ 0 & \frac{\rho_f g\upsilon D}{2eE} & 0 & \frac{-1}{\rho_t c_t^2} \end{bmatrix},$$

$$\mathbf{B}=\begin{bmatrix} 1 & g & 0 & 0 \\ 0 & 0 & -2\upsilon & 0 \\ 0 & 0 & 1 & -1/\rho_t \\ 0 & 0 & -1 & 0 \end{bmatrix}$$

2.2. Solution procedures

This section presents the details of the numerical approaches. For a system of two or more pipes, the same computational time step is used for all elements. In MOC, as already mentioned, the Courant number is 1, so the following equation should be satisfied:

$$Cr=\frac{c_j\Delta t}{\Delta z_j}=\frac{c_j\Delta t}{L_j/n_j}=1\rightarrow \quad n_j=\frac{L_j}{c_j\Delta t}\quad j=1,...,N \quad (9)$$

where L_j=length of pipe j, c_j=wave speed in pipe j, Δt = time step, n_j=number of reaches in pipe j, and N=number of pipes in the system. It is evident that many of the pipes will not satisfy the criteria introduced by Eq. (9) because n_j must be an integer. As a remedy, each pipe separates into two parts: one with proportionate elements and another having a disproportionate section. The proportionate reaches satisfy the Courant number (unity) with the same time step for all pipes. MOC and LF solve the governing equations in proportionate and disproportionate elements in the MOC-LF method, respectively. The location of the disproportionate reaches falls at the end of the pipe. The flow chart of the MOC-LF method is shown in Figure 2. Two computational grids are defined in view of the above element classes: individual cells with spatial grid size ($\Delta z_1, \Delta z_2$) and time step size (

$\Delta t_1, \Delta t_2$). Subscripts 1 and 2 show characteristics of grids for MOC and LF, respectively (see Figure 3). In the last cell of the proportionate section, the variables are computed using MOC, which employs a time step larger than LF. Interpolation is subsequently used to adjust these calculated values to match the smaller time step used by the LF. The MOC-MOC method is similar to the MOC-LF method, but with the difference that the disproportionate element is solved by the MOC. The time step in the disproportionate reaches is smaller than the time step in the proportionate reaches in this method.

2.2.1. MOC approach

MOC has been widely used for transient analysis. This transformation is applied to Eq. (7) as described by Tijsseling (2003; 2009); Li et al. (2003), and also illustrated by Keramat et al. (2012). The governing equations are transformed into ordinary differential equations that can be solved through characteristic lines using finite-difference exactly. The method may also be referred to as diagonalization of the system of partial differential equations. Considering Eq. (7), from $|\mathbf{B} - \lambda \mathbf{A}| = 0$, the eigenvalues λ_i are obtained as:

$$\hat{c}_f = \lambda_1 = -\lambda_2 = \sqrt{\frac{1}{2}(\gamma^2 - \sqrt{\gamma^4 - 4c_f^2 c_t^2})}$$
$$\gamma = c_f^2 + c_t^2 + \upsilon \frac{\rho_f}{\rho_t}\frac{D}{e}c_f^2 \quad (10)$$

$$\hat{c}_t = \lambda_3 = -\lambda_4 = \sqrt{\frac{1}{2}(\gamma^2 + \sqrt{\gamma^4 - 4c_f^2 c_t^2})} \quad (11)$$

Multiplying Eq. (7) by **T**, where $\mathbf{T}=\mathbf{S}^{-1}\mathbf{A}^{-1}$ and **S** represents the matrix of eigenvectors corresponding to the eigenvalues λ_i, allows us to decouple this equation into four independent ordinary differential equations. Consequently, the diagonal matrix of eigenvalues $\mathbf{\Lambda}$ should satisfy the following relation:

$$\mathbf{S}^{-1}(\mathbf{S}^{-1}\mathbf{B})\mathbf{S} = \mathbf{\Lambda} \quad (12)$$

Multiplying by $\mathbf{S}^{-1}$ and using $\mathbf{S}^{-1} = \mathbf{TA}$ results in the following:

$$\mathbf{TB} = \mathbf{\Lambda TA} \quad (13)$$

Using $\mathbf{v} = \mathbf{TAy}$, equation (7) can be rewritten as follows:

$$\frac{\partial \mathbf{v}}{\partial t} + \mathbf{\Lambda}\frac{\partial \mathbf{v}}{\partial z} = 0$$
$$\text{or} \quad \frac{\partial v_i}{\partial t} + \lambda_i \frac{\partial v_i}{\partial z} = 0, \; i=1,2,3,4 \quad (14)$$

The characteristic lines in the distance-time plane satisfy $\lambda_i = \mathrm{d}z/\mathrm{d}t$, so along these lines:

$$\frac{\partial v_i}{\partial t} = 0 \quad (15)$$

Using $\mathbf{v} = \mathbf{S}^{-1}\mathbf{y} = \mathbf{TAy}$, the compatibility Eq. (15) can be expressed in the original unknowns **y**. This relation is then numerically integrated along the relevant characteristic line connecting A1 and A2 with P corresponding to eigenvalues (wave speeds) $\hat{c}_f$ and $-\hat{c}_f$, and A3 and A4 to P corresponding to eigenvalues $\hat{c}_t$ and $-\hat{c}_t$ (see Figure 4). This leads to the following compatibility equations:

$$(\mathbf{TA})_{11}(V_P - V_{A1}) + (\mathbf{TA})_{12}(H_P - H_{A1}) + (\mathbf{TA})_{13}(\dot{u}_{zP} - \dot{u}_{zA1}) + (\mathbf{TA})_{14}(\sigma_{zP} - \sigma_{zA1}) = 0 \quad (16)$$

$$(\mathbf{TA})_{21}(V_P - V_{A2}) + (\mathbf{TA})_{22}(H_P - H_{A2}) + (\mathbf{TA})_{23}(\dot{u}_{zP} - \dot{u}_{zA2}) + (\mathbf{TA})_{24}(\sigma_{zP} - \sigma_{zA2}) = 0 \quad (17)$$

$$(\mathbf{TA})_{31}(V_P - V_{A3}) + (\mathbf{TA})_{32}(H_P - H_{A3}) + (\mathbf{TA})_{33}(\dot{u}_{zP} - \dot{u}_{zA3}) + (\mathbf{TA})_{34}(\sigma_{zP} - \sigma_{zA3}) = 0 \quad (18)$$

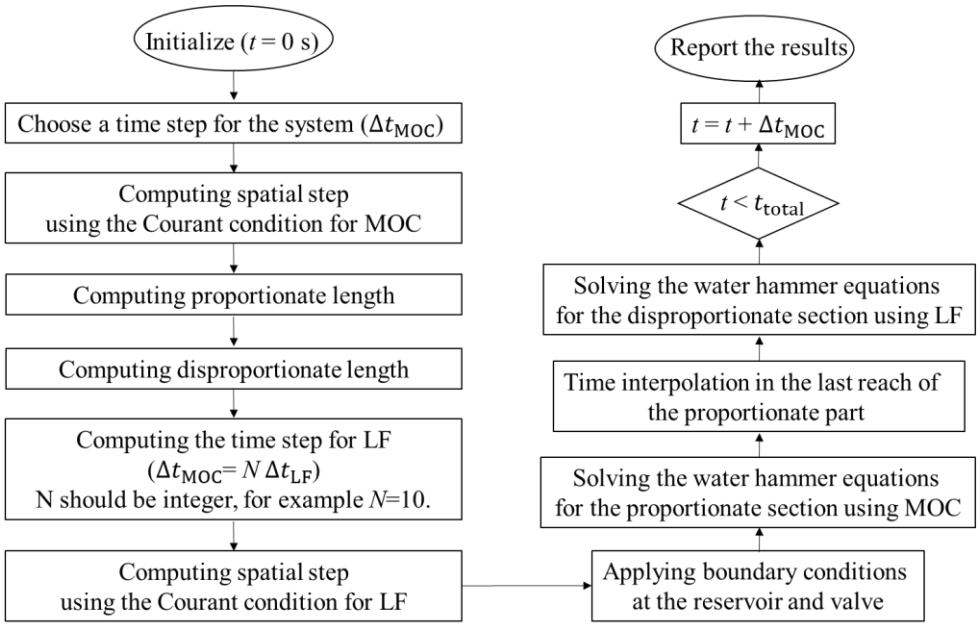

Figure 2. Flow chart of the MOC-LF method.

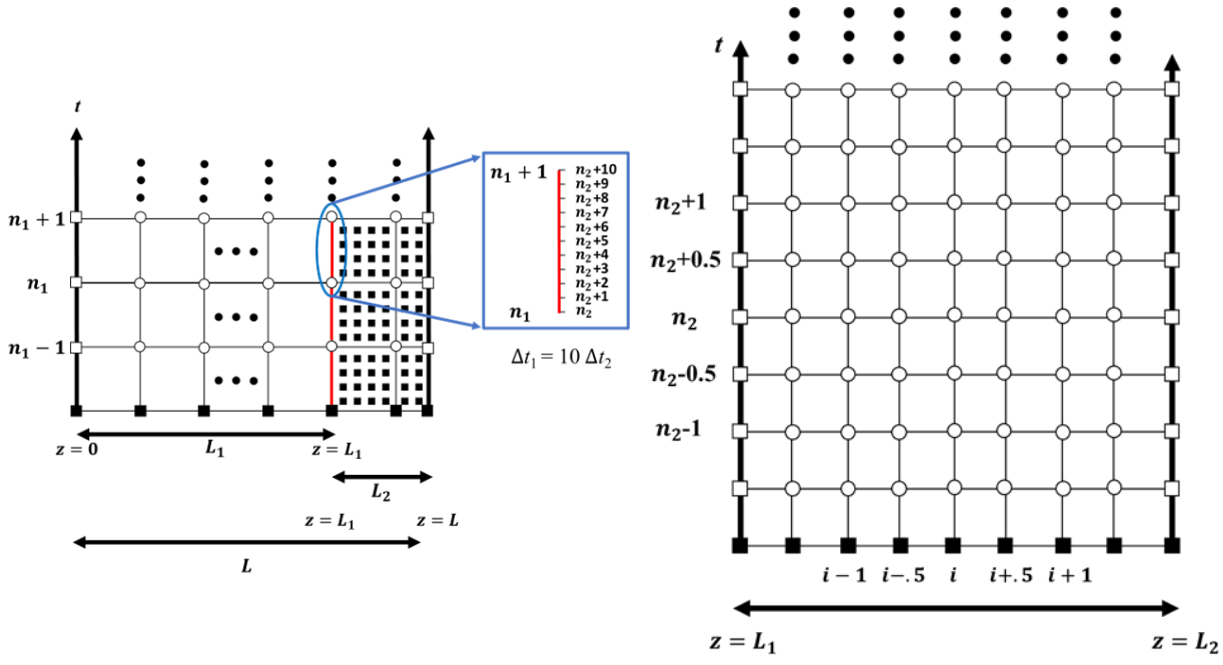

(a) (b)

Figure 3. Schematic representation of computational grids for MOC-LF (L_1 = pipe length in the solution area by MOC, L_2 = pipe length in the solution area by LF, $L = L_1 + L_2$ (a) division of the pipeline into two parts for the MOC and LF implementation, (b) the constructed grids in the LF computations.

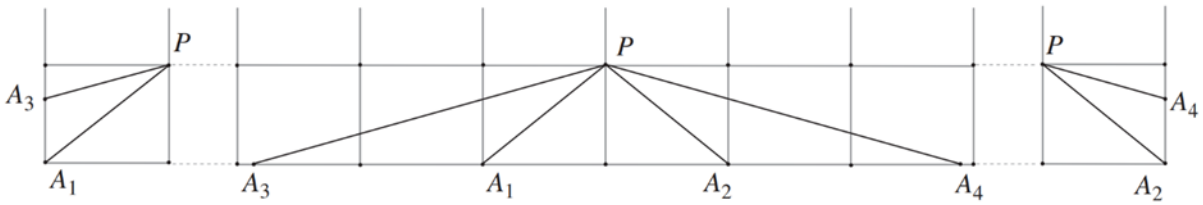

Figure 4. Computational grid based on pressure waves, and characteristic lines for the interior nodes and nodes adjacent to boundaries (Keramat et al., 2012).

$$(\mathbf{TA})_{41}(V_P - V_{A4}) + (\mathbf{TA})_{42}(H_P - H_{A4}) + (\mathbf{TA})_{43}(\dot{u}_{zP} - \dot{u}_{zA4}) + (\mathbf{TA})_{44}(\sigma_{zP} - \sigma_{zA4}) = 0 \quad (19)$$

At the current time step, the unknowns are denoted by P, while A1, A2, A3, and A4 represent the calculated values at the previous time step (Figure 4). The slope of each characteristic line is equal to the inverse of the corresponding wave speed. Here, the numerical time step is aligned with the pressure wave grid ($\Delta t = \Delta z \hat{c}_f$). The components of the **T** matrix in equations (16) - (19) are:

$$T_{11} = T_{21} = 1,\ T_{12} = -T_{22},$$

$$T_{13} = T_{23} = 2\upsilon\left(\hat{c}_f / c_t\right)^2 \left(1 - \left(\hat{c}_f / c_t\right)^2\right)^{-1},$$

$$T_{14} = -T_{24} = 2\upsilon\hat{c}_f \left(1 - \left(\hat{c}_f / c_t\right)^2\right)^{-1},$$

$$T_{31} = T_{41} = \frac{-\rho_f \upsilon D c_f^2}{2eE}\left(1 - \left(\hat{c}_f / c_t\right)^2\right)^{-1}, \quad (20)$$

$$T_{32} = -T_{42} = \frac{-\rho_f \upsilon D c_f^2 \hat{c}_t}{2eE}\left(1 - \left(c_f / \hat{c}_t\right)^2\right)^{-1},$$

$$T_{33} = T_{43} = 1 + \frac{2\rho_f \upsilon^2 D c_f^2}{2eE}\left(1 - \left(c_f / \hat{c}_t\right)^2\right)^{-1},$$

$$T_{34} = -T_{44} = \hat{c}_t$$

At each time step, the Eqs. (16)–(19) along with the boundary conditions using a compatible inverse solution matrix are solved.

Since the grid used is based on pressure waves, the stress wave characteristic lines may not align with grid points from the previous time step (e.g., points A3 and A4 in Figure 4). To address this issue, linear interpolation is employed, using known values from adjacent computational sections on the same time line. Interpolation is performed for points whose characteristic lines do not meet the previous time line, using data from both the current and previous time steps. First, the values of the boundary nodes are obtained, and then the internal nodes are calculated. This sequential process is necessary because the boundary values at the current time step are needed for interpolation.

2.2.2. LF approach

The LF method is based on a piecewise constant approximation of the solution, but it does not require solving a Riemann problem for time advancing, and only uses flux estimates. This method is a prototype of many central schemes (Shampine, 2005; Chikitkin et al., 2015). The advantage of the LF is the simplicity of the algorithm, and the fast and stable calculations. This popular scheme for general non-linear flux functions depends on three basic assumptions: (i) the computational results are replaced with the piecewise constant cell averages at times t^n and $t^n + 0.5\,\Delta t^{n+0.5}$ (ii) there is an upper bound ω on the characteristic speed, so that $\forall \mathbf{y}\ \left|d(\mathbf{By}) / d(\mathbf{Ay})\right| \le \omega$ (iii) the timestep is chosen so that (Trangenstein, 2009):

$$\forall i\ \omega \Delta t^{n+0.5} < \Delta z_i \quad (21)$$

in which $z_i = 0.5(z_{i+0.5} + z_{i-0.5})$ for the grid cell centers. The divergence theorem is applied to Eq. (7) over the space-time rectangle $(z_i, z_{i+1}) \times (t^n, t^n + 0.5\,\Delta t^{n+0.5})$. Since the solution is piecewise constant at time t^n and the timestep is chosen so that waves from the constant states do not reach the cell centers by time $t^n + 0.5$

$\Delta t^{n+0.5}$, the fluxes are constant in time at the cell centers in this application of the divergence theorem:

$$0 = \int_{t^n}^{t^n+0.5\Delta t^{n+0.5}} \int_{z_i}^{z_{i+1}} (\mathbf{A}\frac{\partial \mathbf{y}}{\partial t} + \mathbf{B}\frac{\partial \mathbf{y}}{\partial z})\, dz\, dt \quad (22)$$

$$= \mathbf{A}\int_{z_i}^{z_{i+1}} \mathbf{y}(z, t^n + 0.5\Delta t^{n+1/2})dz - \mathbf{A}\int_{z_i}^{z_{i+1}} \mathbf{y}(z, t^n)dz$$

$$+\mathbf{B}\int_{t^n}^{t^n+0.5\Delta t^{n+1/2}} \mathbf{y}(z_{i+1}, t)\, dt - \mathbf{B}\int_{t^n}^{t^n+0.5\Delta t^{n+1/2}} \mathbf{y}(z_i, t)\, dt$$

$$= \mathbf{A}\int_{z_i}^{z_{i+1}} \mathbf{y}(z, t^n + 0.5\Delta t^{n+1/2})dz - \mathbf{A}[\mathbf{y}_i^n \frac{\Delta z_i}{2} + \mathbf{y}_{i+1}^n \frac{\Delta z_{i+1}}{2}]$$

$$\mathbf{B}\mathbf{y}_{i+1}^n \frac{\Delta t^{n+1/2}}{2} - \mathbf{B}\mathbf{y}_i^n \frac{\Delta t^{n+1/2}}{2}$$

The numerical results are replaced at half-time with the cell averages. A second half-step is similar, applying the divergence theorem over the rectangle $(z_{i\text{-}0.5}, z_{i+0.5})\times(t^n + 0.5\,\Delta t^{n+0.5}, t^n + \Delta t^{n+0.5})$.

The following formulas are obtained for the two half-steps:

$$\mathbf{A}\mathbf{y}_{i+1/2}^{n+1/2} = [\mathbf{A}(\mathbf{y}_i^n \frac{\Delta z_i}{2} + \mathbf{y}_{i+1}^n \frac{\Delta z_{i+1}}{2}) - \mathbf{B}\frac{\Delta t^{n+1/2}}{2}(\mathbf{y}_{i+1}^n - \mathbf{y}_i^n)]\frac{2}{\Delta z_i + \Delta z_{i+1}} \quad (23)$$

$$\mathbf{A}\mathbf{y}_i^{n+1} = \mathbf{A}(\frac{\mathbf{y}_{i-1/2}^{n+1/2} + \mathbf{y}_{i+1/2}^{n+1/2}}{2}) - \mathbf{B}(\mathbf{y}_{i+1/2}^{n+1/2} - \mathbf{y}_{i-1/2}^{n+1/2})\frac{\Delta t^{n+1/2}}{2\Delta z_i} \quad (24)$$

For a uniform grid, $\Delta t = \Delta t^{n+1/2}$ and $\Delta z = \Delta z_i = \Delta z_{i+1}$, Eqs. (23) and (24) become:

$$\mathbf{y}_{i+1/2}^{n+1/2} = \frac{1}{2}(\mathbf{y}_i^n + \mathbf{y}_{i+1}^n) - (\mathbf{A}^{-1}\mathbf{B})\frac{\Delta t}{2\Delta z}(\mathbf{y}_{i+1}^n - \mathbf{y}_i^n) \quad (25)$$

$$\mathbf{y}_i^{n+1} = \frac{1}{2}(\mathbf{y}_{i+1/2}^{n+1/2} + \mathbf{y}_{i-1/2}^{n+1/2}) - (\mathbf{A}^{-1}\mathbf{B})\frac{\Delta t}{2\Delta z}(\mathbf{y}_{i+1/2}^{n+1/2} - \mathbf{y}_{i-1/2}^{n+1/2}) \quad (26)$$

2.2.3. Boundary conditions

In this study, the pipe system consists of a reservoir at the upstream end of the pipeline and a valve at the downstream end discharging to the atmosphere. The location of boundary conditions is shown in Figure 5. The boundary conditions describing a constant reservoir head (H_{Res}) at the connection point to the pipe are:

$$H = H_{\text{Re}s} \quad (27)$$

$$\dot{u}_z = 0 \quad (28)$$

The reservoir is in the range of a proportionate part (MOC).

The valve is in the range of the disproportionate reach. For simulating junction coupling, the free downstream valve of zero mass and with gradual closure are modeled by:

$$\frac{V - \dot{u}_z}{V_0} = \tau\sqrt{\frac{H}{H_0}}, \tau = \frac{(c_d A_V)^{n+1}}{(c_d A_V)_0} \quad (29)$$

$$(\sigma_z - \sigma_{z0})A_t = \rho_f g A_f (H - H_0) \quad (30)$$

Eq. (30) defines the forces balance over the moving valve between the fluid pressure ($\rho_f g A_f (H - H_0)$) and the pipe-wall stress ($(\sigma_z - \sigma_{z0})A_t$). H_0, V_0, and σ_{z0} are steady-state head, velocity and axial pipe stress at the upstream end of the valve, respectively. A_f = cross-sectional discharge area, A_t = cross-sectional pipe wall area. The opening ratio of the valve, τ , is usually defined by the manufacturer over time. It is a function of c_d = discharge coefficient and A_v = opening area of the valve, depending on the valve type and function. In the current simulation, the following function for $\tau(t)$, which is specified based on measurements on a ball-valve is used (Hou et al., 2012):

$$\tau(t)=\begin{cases}(1-(t/T_c))^{3.53} & \text{for } 0\le t\le 0.4T_c\\ 0.394(1-(t/T_c))^{1.7} & \text{for } 0.4T_c\le t\le T_c\\ 0 & \text{for } t\ge T_c\end{cases} \quad (31)$$

in which T_c is the duration of the valve closure. In Poisson coupling only, the valve is fixed to eliminate junction coupling. This means:

$$\dot{u}_z = 0 \quad (32)$$

3. Results and Discussion

3.1. Verification of Numerical Model

The numerical model is built into the MATLAB computer software. To illustrate the proposed method (MOC-LF) and compare its predictions with MOC-MOC and MOC with a very fine grid, two cases are solved numerically based on a reservoir-pipe-valve system.

3.2. Water hammer

The properties of the test problem are: pipe length (L)=1017 m, pipe diameter (D)=50 mm, pressure wave speed (c_f)=1000 m/s, steady-state velocity (V_0)=0.5 m/s, and reservoir head (H_{Res})=45 m. For the generation of the transient, the valve is closed instantaneously and gradually (within 0.2 s).

In Figure 6, the head time history of the valve is plotted for instantaneous valve closure. The results are plotted in a water hammer period ($t=4L/c_f$). The MOC-LF and MOC-MOC predictions are compared with corresponding results of MOC with a very fine grid, which are taken as a reference. The results show a good agreement between the proposed method and the exact solution. As the spatial step size increases (the length of the disproportionate part increases), the difference between the common MOC results and the results of the MOC-LF (and MOC-MOC) gets greater, especially around the discontinuity region, as seen in Figure 7. It should be noted that the MOC profile in the following figures shows the results by solving only the proportionate part of the pipe using the conventional MOC.

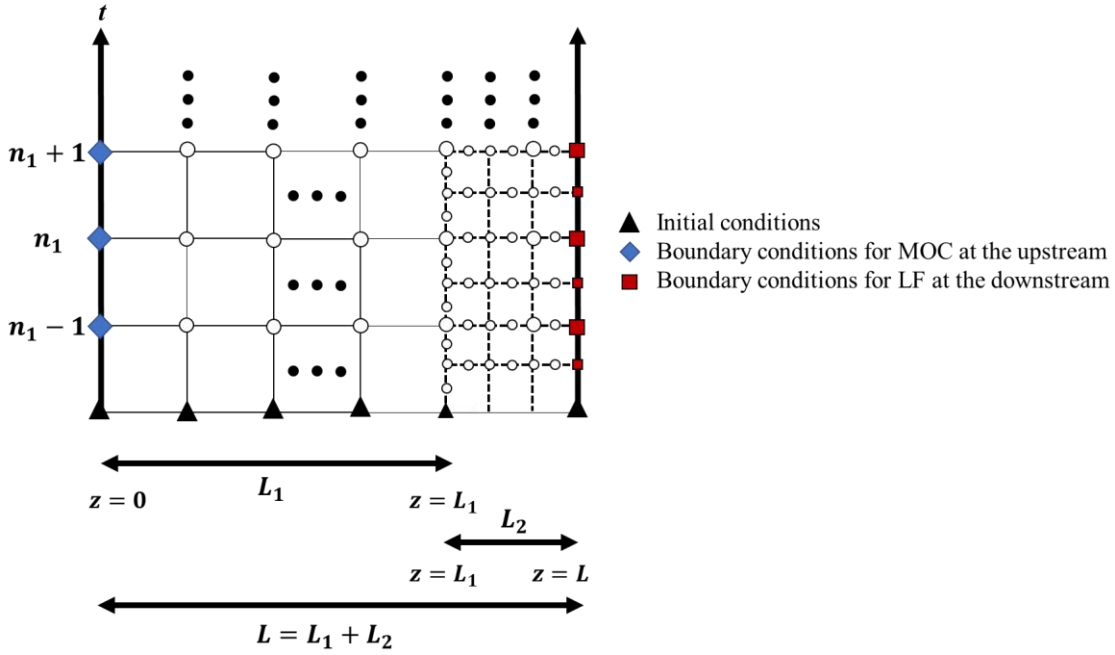

Figure 5. Stencil of initial and boundary conditions for the MOC-LF method.

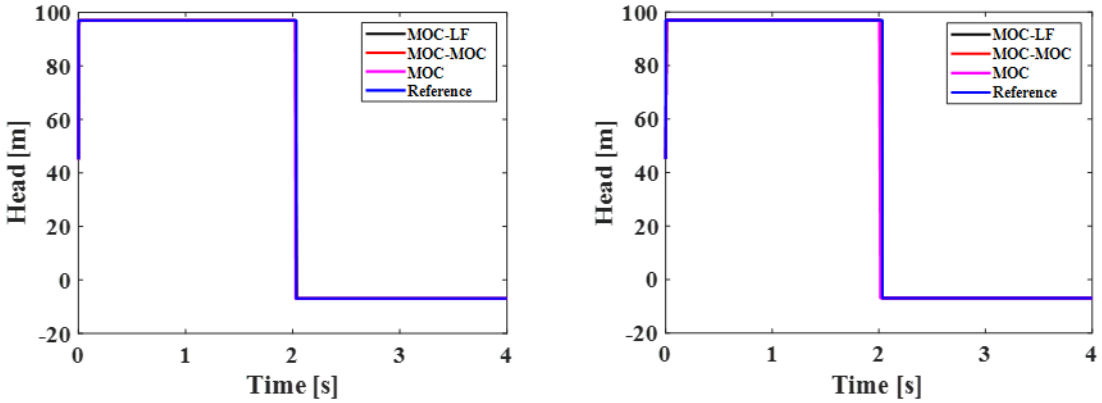

Figure 6. Pressure head comparison of the different methods at the valve ($z = L$) for instantaneous valve closure ($\Delta t_1 = 10\ \Delta t_2$), (a) Δz_1 = 5 m, (b) Δz_1 = 10 m.

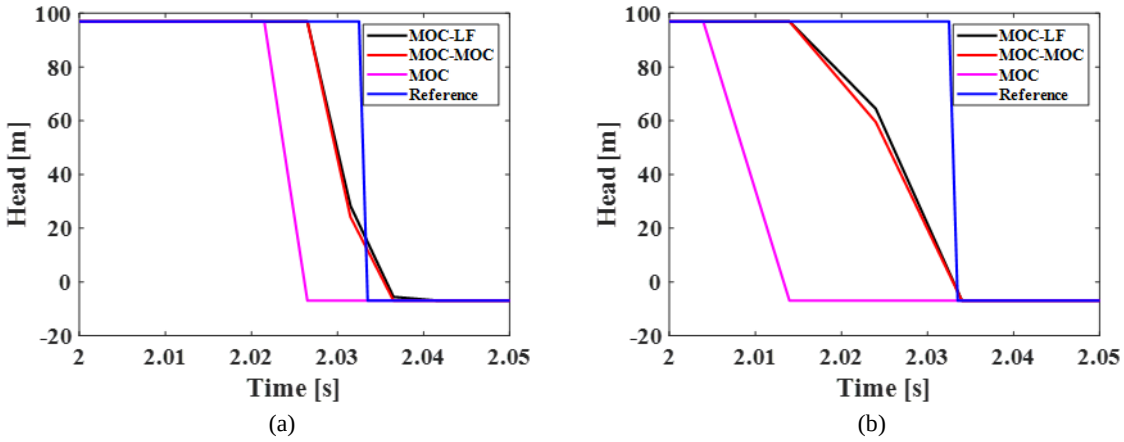

Figure 7. The zoomed picture for Figure 6 in the discontinuous region.

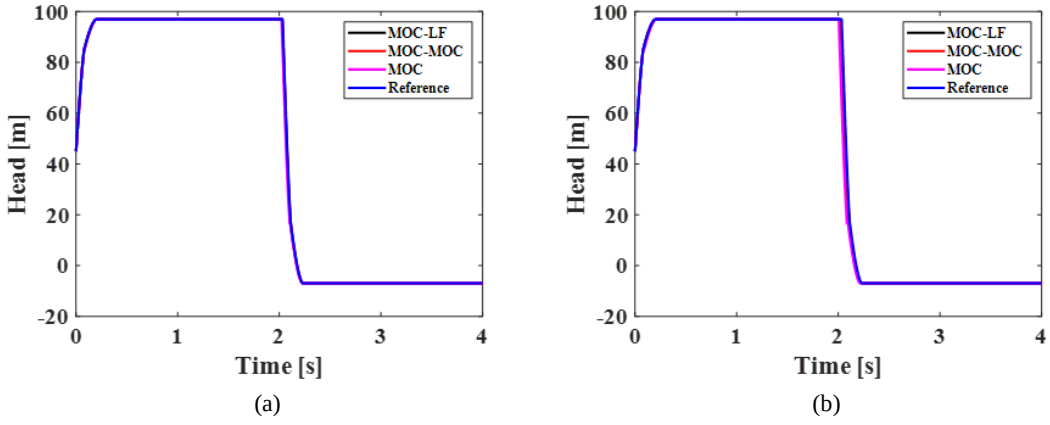

Figure 8. Pressure head comparison of the different methods at the valve ($z = L$) for gradual valve closure ($\Delta t_1 = 10\,\Delta t_2$), (a) Δz_1 = 5 m, (b) Δz_1 = 10 m.

The pressure head results versus time are plotted for gradual valve closure in Figure 8. The results show that MOC-LF and MOC-MOC can simulate head fluctuations with the desired accuracy. Similar to instantaneous valve closure, as the spatial step increases, the difference between the MOC results and the reference results grows.

The model performance is quantified using RMSD for the pressure head.

$$\mathrm{RMSD} = \sqrt{\frac{\sum_{i=1}^{\mathrm{nstep}} (H_i - \hat{H}_i)^2}{\mathrm{nstep}}} \qquad (33)$$

where nstep = number of time steps in a water hammer period; $\hat{H}$ =reference value of pressure head; and H = predicted pressure head using suggested method. Table 1 compares RMSD of conventional MOC, MOC-LF, and MOC-MOC schemes with MOC with a very fine grid for a water hammer period. Conventional MOC with Δz_1=5 m, Δz_1=10 m, and Δz_1 = 15 m simulates pressure head with less accuracy than MOC-LF and MOC-MOC. The origin of this lack of accuracy is ignoring the remaining length, which by increasing this length size, the accuracy of the results decreases. Furthermore, Table 1 demonstrates that the MOC-LF and MOC-MOC results are more accurate in gradual valve closure than those in the case of instantaneous valve closure.

3.3. Fluid-structure interaction

Classical water hammer models do not consider the pipe end movement. This section thus aims to check the accuracy of the proposed method to simulate the effect of pipe-end movements on the pipe response.

The specifications of the test problem are: pipe length (L)=1017 m, pipe diameter (D)=206.4 mm, pipe thickness (e) = 6.35 mm, pipe density (ρ_t)=7900 kg/m3, fluid density (ρ_f)=880 kg/m3, Young's modulus (E)=210 GPa, Poisson's ratio (υ) = 0.3, bulk modulus (K) = 2.1 GPa, steady-state velocity (V_0) = 1 m/s, and reservoir head (H_{Res}) = 0 m. The pressure wave speed (c_f) and axial stress wave speed (c_t) are calculated with Eq. (3) and Eq. (6), respectively. In Figure 9, the computed time histories of the analysis with junction coupling are compared with those of reference. As seen, MOC-LF and MOC-MOC results show agreement with the reference solution.
Figure 10 presents the pressure, velocity, and axial pipe stress predicted by MOC-LF and MOC-MOC for the Poisson coupling. Simulation results are in good accord with reference results.

Table 1. RMSD for instantaneous and gradual valve closure ($\Delta t_1 = 10\,\Delta t_2$).

Method	RMSD (m)					
	Instantaneous			Gradual		
	Δz_1 = 5 (m)	Δz_1 = 10 (m)	Δz_1 = 15 (m)	Δz_1 = 5 (m)	Δz_1 = 10 (m)	Δz_1 = 15 (m)
MOC	8.6	14.0	18.9	2.1	6.2	11.6
MOC-MOC	5.5	8.3	11.1	0.6	1.5	2.7
MOC-LF	5.5	8.7	11.1	0.8	1.9	3.5

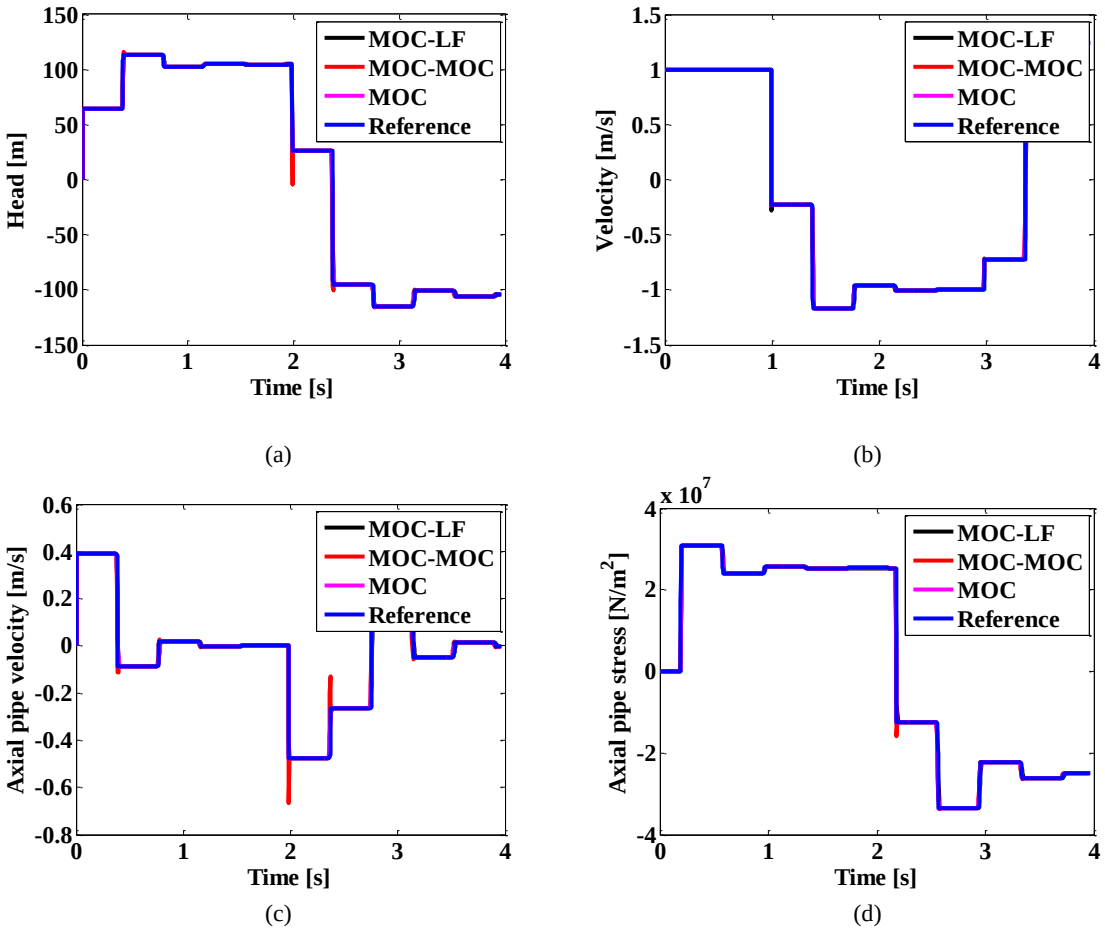

Figure 9. Comparison of the junction coupling results (Δt_1 =10 Δt_2 , Δz_1 = 5 m) using the MOC-LF, MOC-MOC, and the reference solution, (a) pressure head at the valve, (b) velocity at the reservoir, (c) axial pipe velocity at the valve, and (d) axial pipe stress at the reservoir.

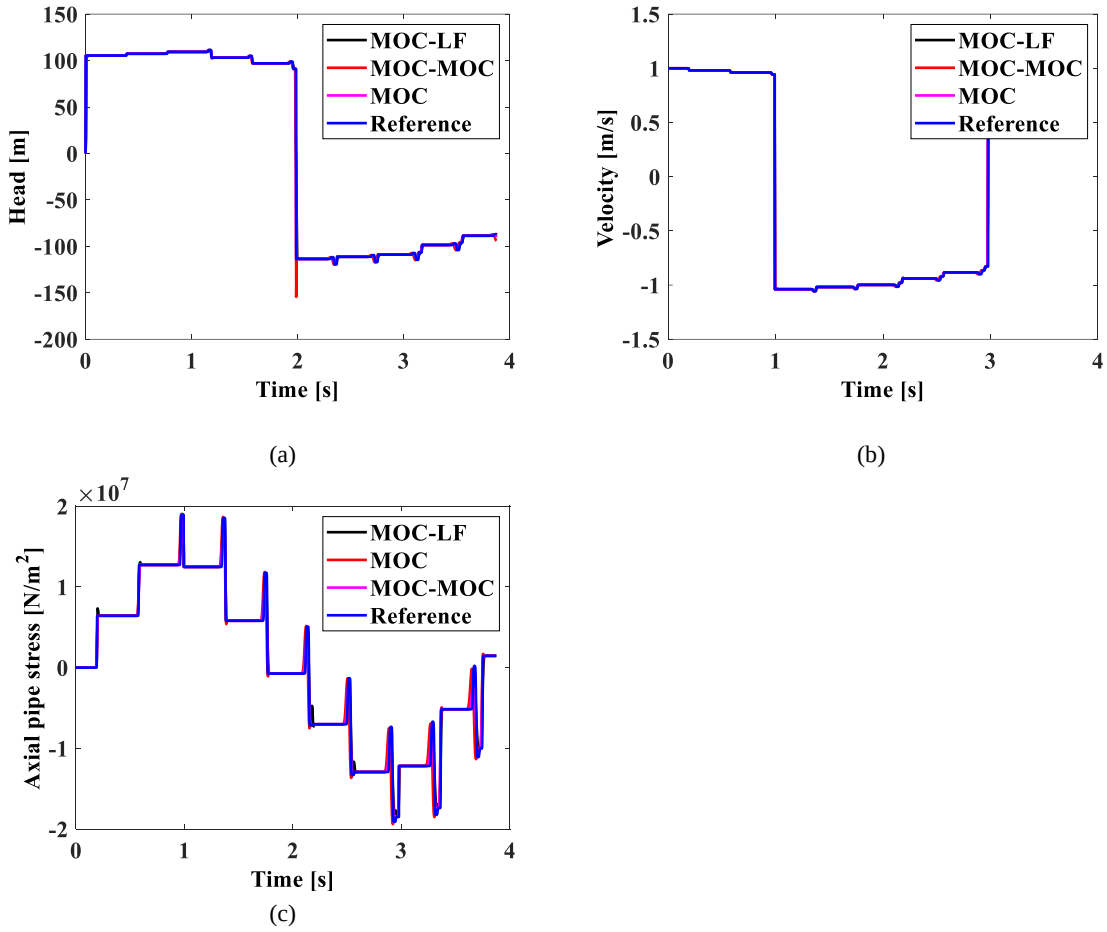

Figure 10. Comparison of the Poisson coupling results (Δt_1 =10 Δt_2 =10, Δz_1 = 5 m) using the MOC-LF, MOC-MOC, and the reference solution, (a) pressure head at the valve, (b) velocity at the reservoir, (c) axial pipe stress at the reservoir.

The RMSD for MOC-LF, MOC-MOC, and conventional MOC with various spatial steps are shown in Table 2. The initial flow velocity is 1 m/s, which results in the Joukowsky pressure of 105 m. The estimated RMSE indicates that the square deviation for the MOC-LF method is quite small in comparison to Joukowsky pressure (RMSD is almost 8% of Joukowsky pressure for Δz_1 = 15 m).

4. Conclusions

This research work investigates the efficiency of the MOC-LF method to simulate the water hammer and fluid-structure including Poisson and junction coupling. The MOC-LF and MOC-MOC methods calculated pressure head variations with time throughout the pipeline, even around discontinuities, with desired accuracy in water hammer simulation. The water hammer results with gradual valve closure have a smaller RMSD than the results of instantaneous valve closure. The FSI results are more accurate in junction coupling than those in the case of Poisson coupling. The MOC-LF method gives very good results and is more accurate than MOC-MOC in FSI simulations. MOC-LF can be an alternative for conventional MOC schemes. The latter method suffers from restrictions on selecting time or space steps.

Table 2. RMSD for FSI with junction and Poisson coupling ($\Delta t_1 = 10\,\Delta t_2$).

Method	RMSD (m)					
	Junction coupling			Poisson coupling		
	Δz_1 = 5 (m)	Δz_1 = 10 (m)	Δz_1 = 15 (m)	Δz_1 = 5 (m)	Δz_1 = 10 (m)	Δz_1 = 15 (m)
MOC	2	5.7	7.0	3.5	9.3	10.4
MOC-MOC	3.5	6.8	9.6	6.0	10.8	12.7
MOC-LF	2	3.6	4.1	3.1	5.6	8.1

Nomenclature

A: Matrices of constant coefficients

B: Matrices of constant coefficients

Cr: Courant number

c: Wave speed

D: Inner pipe diameter

E: Young's modulus for pipe wall material

e: Pipe wall thickness

g: Gravitational acceleration

H: Fluid pressure head

K: Fluid bulk modulus

L: Pipe length

N: Number of pipes in the system

n: Number of reaches in pipe

t: Time

$\dot{u}_z$: Axial pipe velocity

V: Fluid velocity

Δt : Time step

Δz : Spatial step

ρ : Density

σ : Pipe stress

υ : Poisson's ratio

f: Fluid

j: Pipe number

t: Tube, pipe

z: Axial direction

Funding

No funding was received.

Conflicts of Interest

The author declares no conflict of interest.

References

Alatorre, L., Beguería, S., & García-Ruiz, J. M. (2010). Regional scale modeling of hillslope sediment delivery: A case study in the Barasona Reservoir watershed (Spain) using WATEM/SEDEM. *Journal of Hydrology, 391*(1), 109–123.

Bergant, A., Simpson, A. R., & Tijsseling, A. S. (2006). Water hammer with column

separation: A historical review. *Journal of Fluids and Structures, 22*(2), 135–171.

Chikitkin, A. V., Rogov, B. V., & Utyuzhnikov, S. V. (2015). High-order accurate monotone compact running scheme for multidimensional hyperbolic equations. *Applied Numerical Mathematics, 93*(3), 150–163.

El Idrissi, A. Q., da Silva, E. G., & Zeidan, D. (2023). Numerical studies of two-phase water hammer flows using Godunov methods. *Annals of Nuclear Energy, 182*, 109578.

Ferras, D., Manso, P. A., Schleiss, A. J., & Covas, D. I. C. (2017). Fluid-structure interaction in straight pipelines with different anchoring conditions. *Journal of Sound and Vibration, 394*, 348–365.

Ferras, D., Manso, P. A., Schleiss, A. J., & Covas, D. I. C. (2018). One-dimensional fluid–structure interaction models in pressurized fluid-filled pipes: A review. *Applied Sciences, 8*(10), 1844.

Ghodhbani, A., Akrout, M., & Haj Taieb, E. (2019). Coupled approach and calculation of the discrete vapour cavity model. *Journal of Fluids and Structures, 91*, 102691.

Ghidaoui, M. S., & Karney, B. W. (1994). Equivalent differential equations in fixed-grid characteristics method. *Journal of Hydraulic Engineering, 120*(10), 1159–1175.

Ghidaoui, M. S., Karney, B. W., & McInnis, D. A. (1998). Energy estimates for discretization errors in water hammer problems. *Journal of Hydraulic Engineering, 124*(4), 384–393.

Greyvenstein, G. P. (2002). An implicit method for the analysis of transient flows in pipe networks. *International Journal for Numerical Methods in Engineering, 53*(5), 1127–1143.

Henclik, S. (2018). Numerical modeling of water hammer with fluid–structure interaction in a pipeline with viscoelastic supports. *Journal of Fluids and Structures, 76*, 469–487.

Hosseini, R. S., Ahmadi, A., & Zanganeh, R. (2020). Fluid-structure interaction during water hammer in a pipeline with different performance mechanisms of viscoelastic supports. *Journal of Sound and Vibration, 487*, 115527.

Hou, Q., Kruisbrink, A. C. H., Tijsseling, A. S., & Keramat, A. (2012). Simulating water hammer with corrective smoothed particle method. In S. Anderson (Ed.), *Proceedings of the 11th International Conference on Pressure Surges* (pp. 171–187). BHR Group.

Karney, B. W., & Ghidaoui, M. S. (1997). Flexible discretization algorithm for fixed-grid moc in pipelines. *Journal of Hydraulic Engineering, 123*(11), 1004–1011.

Khalighi, F., Ahmadi, A., & Keramat, A. (2016). Investigation of fluid-structure interaction by explicit central finite difference methods. *International Journal of Engineering, 29*(5), 590–598.

Khalighi, F., Ahmadi, A., & Keramat, A. (2017). Water hammer simulation by explicit central finite difference methods in staggered grids. *Journal of Computational & Applied Research in Mechanical Engineering, 6*(2), 69–77.

Keramat, A., Tijsseling, A. S., Hou, Q., & Ahmadi, A. (2012). Fluid–structure interaction with pipe-wall viscoelasticity during water hammer. *Journal of Fluids and Structures, 28*, 434–455.

Lai, C. (1988). Comprehensive method of characteristics models for flow simulation. *Journal of Hydraulic Engineering, 114*(9), 1074–1097.

Laguna, A. J., & Tsouvalas, A. (2014). Transient laminar flow in hydraulic networks based on a semi-analytical impulse response method. *Heron, 59*(1), 37–56.

Li, Q. S., Yang, K., & Zhang, L. (2003). Analytical solution for fluid-structure interaction in liquid-filled pipes subjected to impact-induced water hammer. *Journal of Engineering Mechanics, 129*(12), 1408–1417.

Lu, M., Liu, X., Xu, G., & Tian, Y. (2024). Optimal pump-valve coupling operation strategy of complex long-distance water-conveyance systems based on MOC. *Ain Shams Engineering Journal, 15*(1), 102318.

Pal, S., Hanmaiahgari, P. R., & Karney, B. W. (2021). An overview of the numerical approaches to water hammer modelling: The ongoing quest for practical and accurate numerical approaches. *Water, 13*(11), 1597.

Ramos, H., Tamminen, S., & Covas, D. I. C. (2009). Water supply system performance for different pipe materials Part II: Sensitivity analysis to pressure variation. *Water Resources Management, 23*(2), 367–393.

Samani, H. M. V., & Khayatzadeh, A. (2002). Transient flow in pipe networks. *Journal of Hydraulic Research, 34*(5), 637–644.

Shampine, L. F. (2004). Two-step Lax–Friedrichs method. *Applied Mathematics Letters, 18*(10), 1134–1136.

Shampine, L. F. (2005). Solving hyperbolic PDEs in MATLAB. *Applied Numerical Analysis & Computational Mathematics, 2*(3), 346–358.

Shi, L., Zhang, J., Yu, X. D., Chen, S., Zhao, W. L., & Chen, X. Y. (2023). Water hammer protection for diversion systems in front of pumps in long-distance water supply projects. *Water Science and Engineering, 16*(2), 211–218.

Shimada, M., Brown, J., Leslie, D., & Vardy, A. (2006). Time-line interpolation errors in pipe networks. *Journal of Hydraulic Engineering, 132*(3), 294–306.

Thomas, J. W. (1995). *Numerical partial differential equations: Finite difference methods* (Vol. 22). Springer Science & Business Media.

Tijsseling, A. S. (2003). Exact solution of linear hyperbolic four equation system in axial liquid-pipe vibration. *Journal of Fluids and Structures, 18*(2), 179–196.

Tijsseling, A. S. (2009). Exact computation of the axial vibration of two coupled liquid-filled pipes. *Proceedings of the ASME Pressure Vessels and Piping Division Conference* (Paper PVP2009-77250). ASME.

Trangenstein, J. A. (2009). *Numerical solution of hyperbolic partial differential equations*. Cambridge University Press.

Twyman, J. (2016). Wave speed calculation for water hammer analysis. *Obras y Proyectos, 20*, 86–92.

Twyman, J. (2017). Water hammer analysis using a hybrid scheme. *Revista Ingeniería de Obras Civiles, 7*, 16–25.

Twyman, J. (2018). Water hammer analysis using an implicit finite difference method. *Revista Chilena de Ingeniería, 26*(2), 307–318.

Urbanowicz, K. (2018). Fast and accurate modelling of frictional transient pipe flow. *ZAMM - Journal of Applied Mathematics and Mechanics, 98*(5), 802–823.

Wan, W., Wang, Y., Chen, X., Zhan, H., Wang, T., & Zhang, B. (2023). Investigation of partially expanded surge tank with self-adaptive auxiliary system controlling water hammer in pipelines. *Engineering Science and Technology, an International Journal, 40*, 101379.

Wiggert, D. C., & Sundquist, M. J. (1997). Fixed-grid characteristics for pipeline transients. *Journal of the Hydraulics Division, 103*(12), 1403–1416.

Zhang, B., Wan, W., & Shi, M. (2018). Experimental and numerical simulation of water hammer in gravitational pipe flow with continuous air entrainment. *Water, 10*(7), 928.

Zhang, Q., Liao, T., Ding, L., Wang, K., Yang, H., & Lian, Z. (2023). Study on water hammer effect and tubing string vibration in high-pressure high-production gas wells. *Geoenergy Science and Engineering, 229*, 212147.